

Modeling of Texture Evolution during Hot Forging of Alpha/Beta Titanium Alloys

M.G. GLAVICIC, R.L. GOETZ, D.R. BARKER, G. SHEN, D. FURRER,
A. WOODFIELD, and S.L. SEMIATIN

Texture development during the subtransus hot forging of alpha/beta titanium alloys with an equiaxed-alpha microstructure was modeled using the Los Alamos polycrystalline plasticity (LApp) code and a $\langle 111 \rangle$ pencil-glide polycrystalline plasticity code coupled with the finite-element-method (FEM) program DEFORM. The methodology treated the partitioning of the imposed strain between the alpha and beta phases, and thus enabled the prediction of the distinct deformation textures developed in the primary alpha and beta matrix during hot working. Two variant selection rules in conjunction with the beta deformation texture were also examined to establish a method for predicting the transformation texture of secondary alpha developed as a result of beta decomposition during cooldown following forging or heat treatment. The approach was validated via an industrial-scale trial comprising hot pancake forging of Ti-6Al-4V.

DOI: 10.1007/s11661-007-9376-2

© The Minerals, Metals & Materials Society and ASM International 2008

I. INTRODUCTION

THE modeling of texture evolution during the hot working of two-phase, alpha/beta titanium alloys with a microstructure of equiaxed (primary) alpha in a matrix of beta is complicated by several factors. First, the flow stress behaviors of the hexagonal-close-packed (hcp) alpha phase and the body-centered-cubic (bcc) beta phase differ and exhibit different dependences on temperature. Such differences result in an unequal partitioning of the imposed strain that drives the formation of deformation texture. Second, the beta phase decomposes to form secondary (platelet) alpha during cooling from the hot working (or final heat treatment) temperature. At moderate cooling rates, this phase transformation follows a Burgers-type orientation relationship,

$$\begin{aligned} \{110\}_{\beta} // (0001)_{\alpha} \\ \langle 111 \rangle_{\beta} // [2\bar{1}\bar{1}0]_{\alpha} \end{aligned} \quad [1]$$

in which there are 12 distinct possible variants that can form from a single orientation of a prior beta-phase grain; *i.e.*, the secondary-alpha orientation is related to one of six $\{110\}_{\beta}$ planes, each of which contains two $\langle 111 \rangle_{\beta}$ directions. In addition, the transformation texture

thus formed can vary widely depending upon the initial texture of the beta-phase and any predisposition for one or several of the 12 variants to form preferentially over the others.

The objective of the present work was to develop a modeling framework to describe the evolution of deformation and transformation texture during the thermo-mechanical processing of alpha/beta titanium alloys at temperatures in the two-phase field. For this purpose, numerical techniques to describe strain partitioning and the crystal rotations associated with metal flow and crystal plasticity (*i.e.*, slip) were integrated in a user-friendly manner and validated using an industrial-scale forging of Ti-6Al-4V.

II. BACKGROUND

A brief review of pertinent previous efforts in the area of texture modeling is presented below to provide a background for the methodology used in the present work.

A. Texture Modeling

Several types of models can be used to predict the evolution of crystallographic texture during the large strain deformation of polycrystalline materials. These include the Sachs *isostress* approach,^[1] the Taylor *isostrain* model,^[2] and various crystal plasticity finite-element-method (CPFEM) codes. The Taylor model, which enforces strain compatibility between grains, generally provides the best balance between simplicity and accuracy. It forms the basis for the widely-used Los Alamos polycrystalline plasticity (LApp) code,^[3] which

M.G. GLAVICIC, Research Scientist, R.L. GOETZ, Research Engineer, and D.R. BARKER, Project Manager, are with UES, Inc., Dayton, OH 45432, USA. Contact e-mail: michael.glavicic@wpafb.af.mil G. SHEN, Research Engineer, and D. FURRER, Research Scientist, are with the Rolls-Royce Corporation, Indianapolis, IN 46206-0420, USA. A. WOODFIELD, Senior Scientist, is with General Electric Aviation, Cincinnati, OH 45215, USA. S.L. SEMIATIN, Senior Scientist, is with the Air Force Research Laboratory, Materials and Manufacturing Directorate, AFRL/MLLM, Wright-Patterson AFB, Dayton, OH 45433-7817, USA.

Manuscript submitted June 22, 2007.

Article published online February 16, 2008

can be used to establish the evolution of crystallographic texture in *single-phase* metals during rolling, forging, extrusion, *etc.* However, the Taylor approach does not allow for strain variations from grain-to-grain, let alone within individual grains. When such nonuniformity is important, viscoplastic CPFEM models^[4-6] are applied, but require substantial computer resources and are significantly more complex to apply to the large-strain deformation involved in an actual forging process. Recently, the program ALAMEL^[7] was developed in an attempt to reduce computation requirements; it was applied to model texture evolution during the rolling of interstitial-free steel. In other work, Lebensohn and Canova^[8] developed a viscoplastic self-consistent model to describe texture evolution in alpha/beta titanium alloys with a colony-alpha microstructure. Subsequently, this approach was validated for the simple compression and rolling of the two-phase Fe-Cu system by Commentz *et al.*^[9] Although each of these models shows promise, neither is yet suitable for quantifying texture evolution during the hot forging of complex two-phase alloys in an industrial environment.

B. Modeling of Metal Flow during Forging

Rigid, viscoplastic FEM codes, such as DEFORM*,

*DEFORM 2D, version 8.2, is a trademark of Scientific Forming Technologies Corporation, Columbus, OH.

are now used commonly in the forging industry. Such software has been applied to a variety of nonsteady and steady-state processes to predict the effect of material properties, die design, and process variables on metal flow and the occurrence of defects. Typically, the workpiece material is assumed to be an isotropic continuum (*i.e.*, with a random texture) whose deformation behavior is described by the von Mises criterion and associated flow rule. As a consequence, the development of crystallographic texture is not taken into account, let alone the effect of such texture evolution on the metal flow itself.

C. Coupled Metal Flow-Texture Models

To simplify the problem associated with describing metal flow and texture evolution during large-strain deformation, several research efforts have sought to couple continuum FEM and crystal-plasticity codes. Pérocheau *et al.*^[11] coupled an FEM code with a polycrystalline plasticity model based upon the relaxed-constraints Taylor hypothesis to model the extrusion and rolling of fcc metals. Schoenfeld *et al.*^[12] modeled the through-thickness rolling textures of aluminum by including advanced friction and internal-variable constitutive models into a two-dimensional FEM model developed by Lee *et al.*^[13] More recently, the ALAMEL model,^[7] a statistical-type method with Taylor-type homogenization, was used to model the texture developed in rolled interstitial-free steel.

III. MODELING APPROACH

In a similar fashion to the previous efforts of Van Houtte *et al.*, Pérocheau *et al.*, and Schoenfeld *et al.*^[7,11,12] on single-phase alloys, this present work, in order to analyze texture evolution during the hot forging of two-phase alpha/beta titanium alloys, used a two-dimensional FEM program to analyze crystal rotations due to metal flow and two Taylor *isostrain* models (LApp) code^[3] for the alpha phase and a $\langle 111 \rangle$ *pencil-glide* polycrystalline plasticity code for the beta phase) to quantify rotations due to crystal plasticity. The distinguishing features of the present work related to the treatment of strain partitioning between the phases and its effect on deformation texture evolution, the description of transformation texture and variant selection rules, and the integration of the software packages.

A. Self-Consistent Model of Strain Partitioning

The flow stresses of the individual phases in alpha/beta titanium alloys such as Ti-6Al-4V are very different at the temperatures typically used during hot forging, *i.e.*, 800 °C to 975 °C. The alpha phase is approximately 3 times as strong as the beta phase.^[14] In addition, the volume fraction of the phases varies greatly. For example, the volume fraction of alpha varies from ~80 pct at 800 °C to ~20 pct at 975 °C. Hence, the strain accommodated by the alpha and beta phases is not equal and may be expected to vary with temperature. Thus, an analytical method to quantify the strain accommodated by each phase is required to model the texture change associated with crystal plasticity. In the present work, a simple self-consistent approach^[14] was adopted. This method is based on the technique developed by Hill^[15] and later extended by Suquet^[16] for linearly-elastic solids. Hill's analysis assumed that both phases are linearly viscoplastic; *i.e.*, they each have a constitutive relation of the form:

$$\sigma_i = k_i^L \dot{\epsilon}_i \quad [2]$$

in which σ and $\dot{\epsilon}$ denote the flow stress and strain rate, respectively, k^L is the "viscosity" coefficient, and the subscripts ($i = 1, 2$) refer to phases 1 or 2. The viscosity of the aggregate k_{sc}^L (which relates the aggregate flow stress and strain rate) is given by the following expression:

$$k_{sc}^L/k_1^L = (1/6) \left\{ 3 - 2\rho + 5(1-f)(\rho-1) + \sqrt{[3 - 2\rho + 5(1-f)(\rho-1)]^2 + 24\rho} \right\} \quad [3]$$

in which $\rho = k_2^L/k_1^L$, and f denotes the volume fraction of phase 1.

Suquet^[16] extended the preceding analysis to the case in which both phases are power-law viscoplastic, *viz.*

$$\sigma_i = k_i \dot{\epsilon}_i^{m_i} \quad [4]$$

and the strain-rate sensitivity exponents for both phases are equal; *i.e.*, $m_1 = m_2 = m$. In this case, the viscosity-like parameter of the aggregate (k) is a

function of the values of viscosity-like parameters for the two phases, k_1 and k_2 , as well as m , ρ , and k_{sc}^L/k_1^L :

$$k/k_1 = \frac{\min}{\rho \geq 0} \left\{ \left(k_{sc}^L/k_1^L \right)^{(m+1)/2} \times \left[f + (1-f)\rho^{(m+1)/(m-1)} \times \left(k_2/k_1 \right)^{2/(1-m)} \right]^{(1-m)/2} \right\} \quad [5]$$

In Eq. [5], the expression on the right-hand side before the argument in braces denotes the minimum value for $\rho \geq 0$. In practice, the value of k_{sc}^L/k_1^L for the corresponding linearly-viscous case is unknown. Thus, the evaluation of k/k_1 involves a procedure in which trial values of ρ are guessed, k_{sc}^L/k_1^L is determined from Eq. [3], and ρ and k_{sc}^L/k_1^L are inserted into Eq. [5]. The value of ρ that yields the minimum value of k/k_1 is the appropriate one.

The *average* strain rates in the two phases are readily calculated from the values of k , k_1 , k_2 , and the volume fraction f of phase “1”. Following Hill,^[17] the aggregate flow stress σ_{ov} and strain rate $\dot{\epsilon}_{ov}$ are volume averages of the corresponding flow stresses and strain rates in the individual phases:

$$\sigma_{ov} = k\dot{\epsilon}_{ov}^m = f k_1 \dot{\epsilon}_1^m + (1-f) k_2 \dot{\epsilon}_2^m \quad [6]$$

$$\dot{\epsilon}_{ov} = f \dot{\epsilon}_1 + (1-f) \dot{\epsilon}_2 \quad [7]$$

Solving Eq. [7] for $\dot{\epsilon}_2$ as a function of $\dot{\epsilon}_{ov}$ and $\dot{\epsilon}_1$,

$$\dot{\epsilon}_2/\dot{\epsilon}_{ov} = [1 - f(\dot{\epsilon}_1/\dot{\epsilon}_{ov})]/(1-f) \quad [8]$$

Inserting this relation into Eq. [6], an expression for $\dot{\epsilon}_1/\dot{\epsilon}_{ov}$ is obtained:

$$k/k_1 = f \left(\dot{\epsilon}_1/\dot{\epsilon}_{ov} \right)^m + \left[(1-f)^{(1-m)} \left(k_2/k_1 \right) \left(1 - f \left(\dot{\epsilon}_1/\dot{\epsilon}_{ov} \right) \right)^m \right] \quad [9]$$

Equation [9] cannot be solved analytically, but is readily evaluated using numerical techniques.

From Eqs. [8] and [9], the strain rates and hence strain increments for each phase are determined as a function of their relative flow stresses and volume fractions. The strain increments so determined were used in crystal-plasticity-model calculations to estimate rotations due to slip.

B. Beta-Phase Decomposition

At relatively slow cooling rates following hot forging (or heat treatment) of titanium components (*i.e.*, < 20 °C/min), primary alpha particles grow epitaxially, consuming the majority of the beta matrix.^[8] At faster cooling rates (between ~ 20 °C/min and 200 °C/min), typical of fan cooling or water quenching of finite-section-size workpieces, the beta matrix decomposes at a critical supersaturation to form colonies of secondary-alpha platelets,^[18] each of which possess a Burgers-orientation relation with its parent beta matrix (Eq. [1]).

The texture associated with the secondary-alpha phase can vary greatly depending on which of the 12 possible variants is selected during beta-phase decomposition. The manner in which a beta-phase orientation is transformed is governed by the relationship

$$DS_k^\beta B = A \quad [10]$$

in which D is a rotation matrix, defined by the Euler angles $\varphi_1 = 135$, $\Phi = 90$, and $\varphi_2 = 325$,^[19] S_k^β is a subset of the cubic symmetry operators (Table I); B is the beta-phase orientation matrix; and A is the alpha phase orientation matrix.

In the present work, the secondary alpha of interest was formed during rapid cooling following solution treatment of a forging high in the alpha-beta phase field. Two different variant-selection possibilities were examined. These rules were based on the previous experimental observations for commercial-purity titanium^[20–22] and Ti-6Al-4V.^[23–25]

In the first case, all variants were assumed to be equally likely. In this instance, a specific rotation matrix S_k^β from Table I was randomly selected from the 12 possibilities for the transformation of each individual beta-phase orientation.

Table I. Subset of Cubic Symmetry Operators Used to Transform the Beta Phase into Distinct Alpha-Phase Variants

| | | |
|---|---|--|
| $S_1^\beta = \begin{bmatrix} 1 & 0 & 0 \\ 0 & 1 & 0 \\ 0 & 0 & 1 \end{bmatrix}$ | $S_5^\beta = \begin{bmatrix} 0 & -1 & 0 \\ 0 & 0 & -1 \\ 1 & 0 & 0 \end{bmatrix}$ | $S_9^\beta = \begin{bmatrix} 0 & 0 & 1 \\ -1 & 0 & 0 \\ 0 & -1 & 0 \end{bmatrix}$ |
| $S_2^\beta = \begin{bmatrix} 0 & 0 & 1 \\ 1 & 0 & 0 \\ 0 & 1 & 0 \end{bmatrix}$ | $S_6^\beta = \begin{bmatrix} 0 & 1 & 0 \\ 0 & 0 & -1 \\ -1 & 0 & 0 \end{bmatrix}$ | $S_{10}^\beta = \begin{bmatrix} -1 & 0 & 0 \\ 0 & 1 & 0 \\ 0 & 0 & -1 \end{bmatrix}$ |
| $S_3^\beta = \begin{bmatrix} 0 & 1 & 0 \\ 0 & 0 & 1 \\ 1 & 0 & 0 \end{bmatrix}$ | $S_7^\beta = \begin{bmatrix} 0 & 0 & -1 \\ 1 & 0 & 0 \\ 0 & -1 & 0 \end{bmatrix}$ | $S_{11}^\beta = \begin{bmatrix} -1 & 0 & 0 \\ 0 & -1 & 0 \\ 0 & 0 & 1 \end{bmatrix}$ |
| $S_4^\beta = \begin{bmatrix} 0 & -1 & 0 \\ 0 & 0 & 1 \\ -1 & 0 & 0 \end{bmatrix}$ | $S_8^\beta = \begin{bmatrix} 0 & 0 & -1 \\ -1 & 0 & 0 \\ 0 & 1 & 0 \end{bmatrix}$ | $S_{12}^\beta = \begin{bmatrix} 1 & 0 & 0 \\ 0 & -1 & 0 \\ 0 & 0 & -1 \end{bmatrix}$ |

In the second case, $\langle 111 \rangle$ pencil-glide in the beta phase during cooling from the final solution heat treatment was assumed to control variant selection. Here, the methodology developed by Morris and Semiatin^[26] was used to determine the $\langle 111 \rangle$ slip directions and slip planes activated to accommodate the strain increments developed during cooling, as predicted by FEM analysis. From the two closest $\{110\}$ planes that could have equivalently accommodated this same shear strain *via* $\langle 111 \rangle$ pencil-glide (Figure 4 in Reference 26), the $\{110\}\langle 111 \rangle$ slip system on which the highest resolved shear stress had been developed was assumed to comprise the plane/direction that determined the orientation of the selected alpha variant. Because the variants of the alpha phase are assumed to form per the Burgers relationship (Eq. [1]), the resolved shear stress τ on a given $\{110\}\langle 111 \rangle$ slip system in the beta phase for a given imposed stress state will be the same as the resolved shear stress on the $(0001)[2\bar{1}\bar{1}0]$ slip system in the alpha phase after the phase transformation. The equivalent slip planes/directions of the beta and alpha phase are then related by

$$\tau = m_{\beta}^{(s)} : B\sigma B^T = m_{\alpha}^{\text{basal}(a)} : A\sigma A^T \quad [11]$$

in which $m_{\beta}^{(s)}$ and $m_{\alpha}^{\text{basal}(a)}$ are the tensor quantities $m_{ij}^{(s)} = 1/2[\hat{b}_i\hat{n}_j + \hat{b}_j\hat{n}_i]$, in which the slip direction \hat{b} and slip plane normal \hat{n} are defined by $\{110\}\langle 111 \rangle$ slip systems of the beta phase and the $(0001)[2\bar{1}\bar{1}0]$ slip system of the alpha phase. Inserting Eq. [10] into Eq. [11],

$$m_{\beta}^{(s)} : B\sigma B^T = m_{\alpha}^{\text{basal}(a)} : DS_k^{\beta} B\sigma (DS_k^{\beta} B)^T \quad [12]$$

permits the specific alpha phase variant $DS_k^{\beta} B$ that has the same resolved shear stress as in the beta phase to be selected from the 12 possible variants and used to transform the beta phase orientation.

C. Calculation Procedures and Integration of Software Packages

Current CPFEM codes are too demanding from a computational standpoint to model texture evolution at every material point during the forging of a single-phase alloy, let alone for a complex forging of a two-phase material. Thus, the present work consisted of a decoupled approach in which crystal rotations due to metal flow and crystallographic slip were treated separately, thereby providing a compromise between scientific rigor and user-friendliness in an industrial environment. To this end, the FEM metal-flow program DEFORM and the two crystal-plasticity codes (LApp^[3] and the $\langle 111 \rangle$ pencil-glide model of Morris and Semiatin^[26]) were selected. In addition to these software packages, other specially developed codes were incorporated into a series of user-friendly GUIs that could be easily operated.

Model calculations consisted of running DEFORM in the usual manner. After the DEFORM simulation was run, the strain increments and *metal-flow-related* rotation for each time step and FEM node (integration

point) was output in the form of a set of ASCII files. The strain increments were partitioned per the approach described in Section A of this article and used as input to separate alpha-phase and beta-phase calculations of the slip-related rotations. For the alpha phase, LApp^[3] was used to model the texture evolution, whereas for the beta phase, the Morris and Semiatin $\langle 111 \rangle$ pencil-glide approach^[26] was used. The crystal plasticity input also included experimental pole-figure data from X-ray, neutron diffraction, or electron backscatter diffraction (EBSD) measurements, obtained using the Los Alamos preferred orientation package (popLA)^[3] and other internally developed software. After each strain increment, the texture change (equal to the sum of the metal-flow and LApp/ $\langle 111 \rangle$ pencil-glide-calculated, slip-related rotations) was imposed at each node for each phase. The resulting texture was then used as the initial texture for the next increment of deformation.

Subsequent to the crystal plasticity calculations, an additional FEM simulation was performed to model the quenching procedure that followed the final heat treatment of a pancake forging used as the validation example. The predicted beta-phase texture was then converted to a secondary-alpha texture using each of the two possible variant-selection rules using the stresses and strains predicted to have been developed at the median temperature (~ 810 °C), at which secondary alpha would have been expected to nucleate during quenching.^[28] The predicted primary-alpha (deformation) texture and secondary-alpha (transformation) texture were then weighted per the relative volume fractions of the phases and then added to obtain the overall alpha-phase texture. The volume fraction of primary alpha is a function of the forging temperature and the cooling rate; it can be estimated using a simple diffusion analysis.^[18,28] The volume fraction of secondary alpha was then taken to be the difference between the total alpha content (typically of the order of 0.95 for alloys such as Ti-6Al-4V) and the primary-alpha volume fraction. Alternatively, EBSD techniques, such as that described by Germain *et al.*,^[29] can be used to separate the primary- and secondary-alpha constituents.

IV. MATERIALS AND EXPERIMENTAL PROCEDURES

The texture developed during the final heat treatment of a Ti-6Al-4V pancake forging was used to validate the modeling approach described in Section III.

A. Material

The validation material comprised a 280-mm-diameter Ti-6Al-4V billet that had a composition (in wt pct) of 6.62 aluminum, 4.10 vanadium, 0.19 oxygen, 0.007 nitrogen, 0.02 carbon, and 0.004 hydrogen, with the balance titanium. The initial microstructure of the billet material at the forging preheat temperature (955 °C) consisted of equiaxed, primary-alpha particles in a matrix of the beta phase (Figure 1).

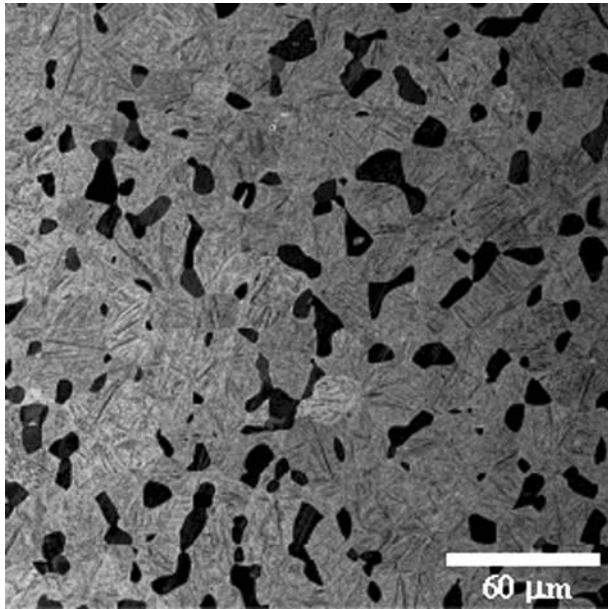


Fig. 1—Backscattered-electron image of microstructure developed in Ti-6Al-4V at 955 °C followed by water quenching. The dark, equiaxed phase is primary alpha. The gray, transformed phase was beta at the heat-treatment temperature.

The variation of the volume fraction of beta with temperature (the so-called beta-approach curve), which was needed for both the strain-partitioning calculations and the determination of the overall alpha-phase texture, was determined using PANDAT** and its

**PANDAT is a trademark of Computherm LLC, Madison, WI.

associated titanium database. The beta-approach curve between 700 °C and the beta-transus temperature (~995 °C) was fit to a seventh-order polynomial function.

B. Experimental Procedures

The validation trial comprised the hot-die forging of a cylindrical billet with initial dimensions of 280-mm diameter × 510-mm height. The preform was coated with glass, preheated at 955 °C, and forged to a 70 pct height reduction between flat tool-steel dies preheated to approximately 600 °C to minimize workpiece chilling. Forging was conducted in a hydraulic press at a constant crosshead speed to produce a nominal strain rate of 0.7 s⁻¹. With the prescribed die and billet temperatures and deformation rate, it was estimated that the preform temperature remained between 870 °C and 955 °C and that deformation heating at the center of the preform did not play a significant role. Immediately following forging, the pancake was water quenched. Subsequently, the forging was given a final heat treatment at a temperature 30 °C below the beta transus for 1 hour and water quenched.

The forging and quenching operations were modeled using DEFORM. The point-tracking feature within the software was used to identify the local strain increments, metal-flow rotation, and cooling transients (during water quenching) at six specific locations within the pancake (Figures 2 and 3).

Specimens extracted from the pancake forging at the six tracking-point locations were metallographically prepared for microstructural characterization and texture measurement. The textures in the final forging, as well as at the corresponding locations in the starting billet, were quantified using X-ray diffraction to establish (10 $\bar{1}$ 0), (0002), (10 $\bar{1}$ 1), (10 $\bar{1}$ 2), and (11 $\bar{2}$ 0) alpha-phase pole figures and (110) and (200) beta-phase pole figures. The pole figures were measured in the Schultz-reflection mode using Cu K α radiation. Analysis of the measured data was performed using popLA. The input

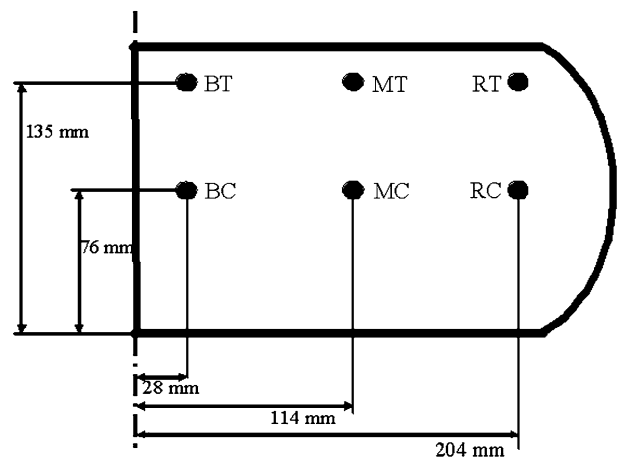


Fig. 2—Specimens extracted from the Ti-6Al-4V pancake forging for microstructure and texture examination. BC: bore-midplane, MC: midradius-midplane, RC: rim-midplane, BT: bore-top, MT: midradius-top, and RT: rim-top locations.

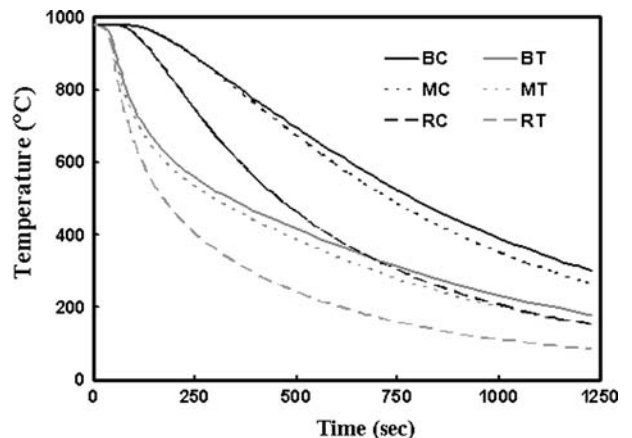


Fig. 3—FEM-model predictions of temperature transients at different locations in the pancake forging during quenching following final heat treatment.

to crystal-plasticity codes for the deformation-texture simulations consisted of the initial textures and slip modes. To model the evolution of texture in the primary-alpha phase, LApp^[3] was used and deformation was assumed to be possible *via* basal $\langle a \rangle$, prism $\langle a \rangle$, and pyramidal $\langle c + a \rangle$ slip with a ratio of the corresponding critical-resolved shear stresses of 1, 0.7, and 3, respectively. For the beta phase, deformation *via* $\langle 111 \rangle$ pencil-glide was modeled using the methodology of Morris and Semiatin.^[26]

In order to gage the accuracy of the modeling capability for the alpha-phase *deformation* texture alone, a specimen from the RT location in the forging was taken to the final heat treatment temperature and then furnace cooled to produce a structure that was essentially fully equiaxed alpha. Pole figure measurements for this sample were made in the same manner as the other samples.

V. RESULTS AND DISCUSSION

A. Microstructure Observations

Following the final heat treatment, a variety of bimodal microstructures was developed in the forging (Figure 4). The different microstructures can be ascribed to the variation in local cooling rate (Figure 3), the

supersaturations that were developed, and the temperature at which the secondary alpha was formed.^[18] At the bore-midplane location BC, as shown in Figure 4(a), for example, a bimodal microstructure of equiaxed alpha in a transformed matrix of coarse, colony (secondary) alpha was formed. The microstructure was similar at the top of the bore location BT (Figure 4(c)), despite the somewhat faster cooling rate at BT compared to that at BC (Figure 3). At the rim-midplane location RC (Figure 4(b)), the secondary alpha was somewhat finer even though the cooling rate here (Figure 3) was estimated to be between that of the bore-midplane and bore-top locations. A much finer microstructure was formed at the rim-top region RT (Figure 4(d)); higher magnification micrographs revealed that the secondary alpha here had a basket-weave morphology with a formation that could be explained by the very fast cooling rate, deduced from the FEM simulations (Figure 3). In general, the variation of the volume fraction of primary alpha with location (Table II) corresponded to the cooling rate; *i.e.*, slower cooling rates led to a greater tendency for epitaxial growth of primary alpha and hence a greater final fraction of this constituent. On the other hand, a more detailed analysis appears to be needed to explain the details of the formation and thickening of secondary-alpha plates.

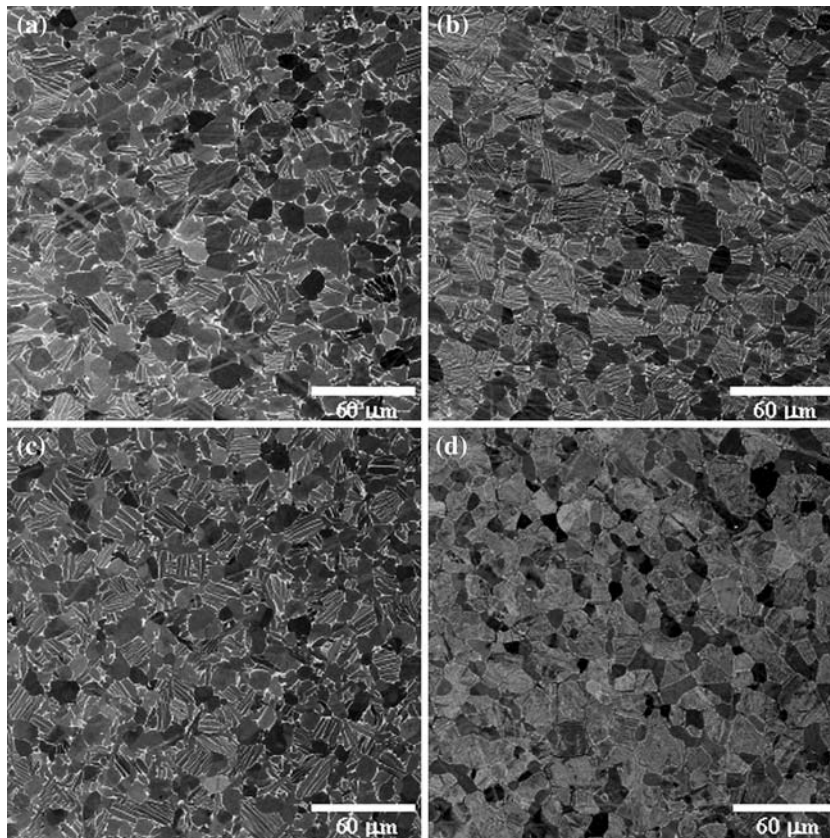


Fig. 4—Backscattered-electron images of microstructures developed in the Ti-6Al-4V pancake forging following water quenching from the final heat treatment at the (a) BC, (b) RC, (c) BT, and (d) RT locations.

Table II. Dependence of the Volume Fraction of Primary Alpha and Effective Strain on Location in the Pancake Forging

| Location | Volume Fraction of Primary Alpha (Pct) | Effective Strain |
|----------|--|------------------|
| BC | 46 | 2.635 |
| MC | 48 | 2.011 |
| RC | 42 | 1.266 |
| BT | 38 | 0.055 |
| MT | 39 | 0.599 |
| RT | 30 | 1.105 |

B. Texture Measurements and Model Predictions

The texture developed in the pancake forging also varied from location to location. At the BC location, shown in Figure 5(a), and other locations along the axis of the pancake, an axisymmetric texture was formed for the primary + secondary alpha phases. The textures predicted using the FEM stresses and strain increments developed at 810 °C (Figure 6) showed that specific features in the measured pole figures could be explained with the variant selection rules chosen, as depicted in Figures 5(b) and (c).

In the case for which all variants were considered possible, shown in Figure 5(b), a pole appeared at the 6 o'clock and 12 o'clock positions in the (11 $\bar{2}$ 0) pole figure and a fiber along the horizontal equatorial plane of the (0002) pole figure. Moreover, fiber textures above and below the horizontal equatorial planes of the (0002) and (11 $\bar{2}$ 0) pole figures were also predicted. These features were also observed in the measured pole figures, as shown in Figure 5(a).

For the $\langle 111 \rangle$ pencil-glide variant-selection approach, which allowed several variants to form from a single

beta orientation, shown in Figure 5(c), the fiber textures above and below the horizontal equatorial planes of the (0002) and (11 $\bar{2}$ 0) pole figures were more pronounced. Moreover, two strong poles appeared diagonally in the (0002) and (11 $\bar{2}$ 0) pole figures. The corresponding measured pole figures, shown in Figure 5(a), also showed poles at these locations, suggesting possibly that slip system activity may influence which variants will form. This result is similar to that found in the work of Gey *et al.*,^[24] who were able to correlate alpha-variant selection following rolling in the beta-phase field to the most active $\{110\}\langle 111 \rangle$ and $\{211\}\langle 111 \rangle$ slip systems. However, the lack of predicted poles at the 6 o'clock and 12 o'clock positions in the predicted (11 $\bar{2}$ 0) pole figure indicates that this variant-selection approach cannot explain a number of the features observed in the measured pole figures, shown in Figure 5(a).

A (0002) fiber-texture component, as seen by the poles at the 12 o'clock and 6 o'clock positions in the (0002) pole figure and the maximum along the horizontal equatorial plane in the (11 $\bar{2}$ 0) pole figure, was also predicted using both variant selection rules, as seen in Figures 5(b) and (c). As may be seen in Figure 5(a); unfortunately, these types of texture components were not observed in the experimental data. Hence, further work is required to ascertain the origins of this texture component.

As shown in Figure 7(a), at other locations in the pancake forging for which there was significant rotation due to metal flow, such as RT, a more complex texture was formed. The stresses and strain increments developed at this location (Figure 8) were dissimilar to those developed at the BC location (Figure 6). Using the stresses and strains developed at 810 °C and the variant selection rules based on $\langle 111 \rangle$ pencil-glide activity, model predictions, shown in Figure 7(c), did not successfully

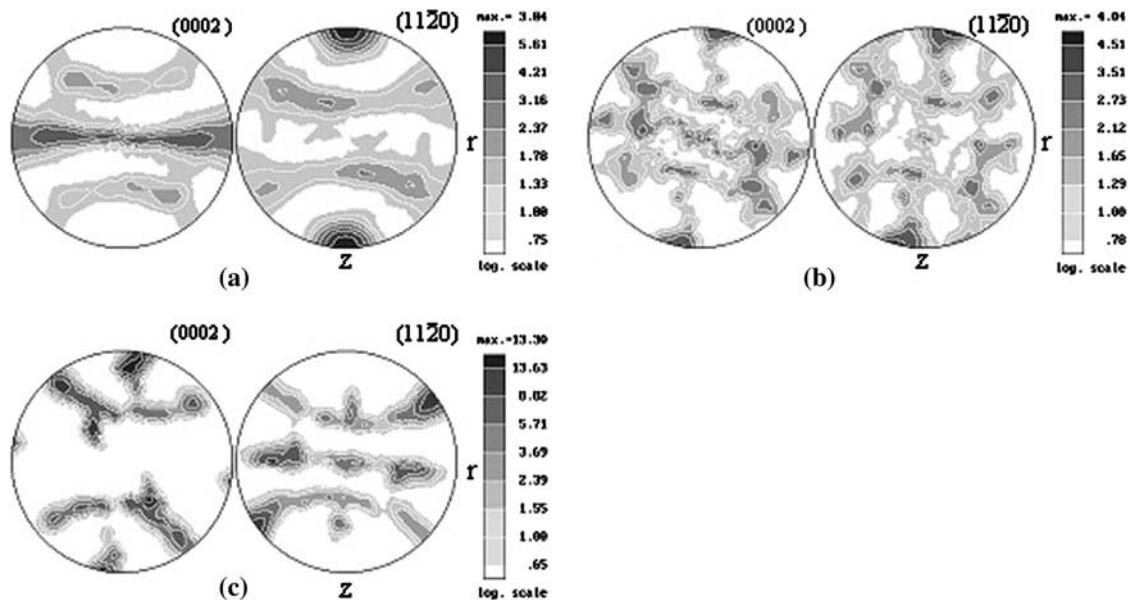


Fig. 5—Alpha-phase pole figures for the BC location following forging and heat treatment: (a) measured, (b) simulated with all variants, and (c) simulated with preferential variant selection based on $\langle 111 \rangle$ pencil-glide.

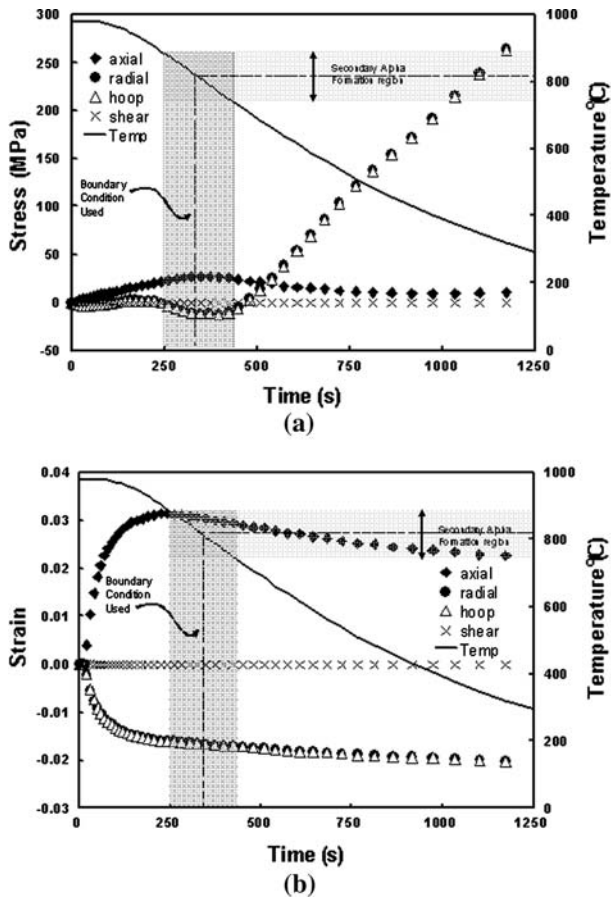


Fig. 6—FEM predictions at the BC location: (a) stress and (b) strain components and temperature as a function of time during water quenching following solution heat treatment of the forging.

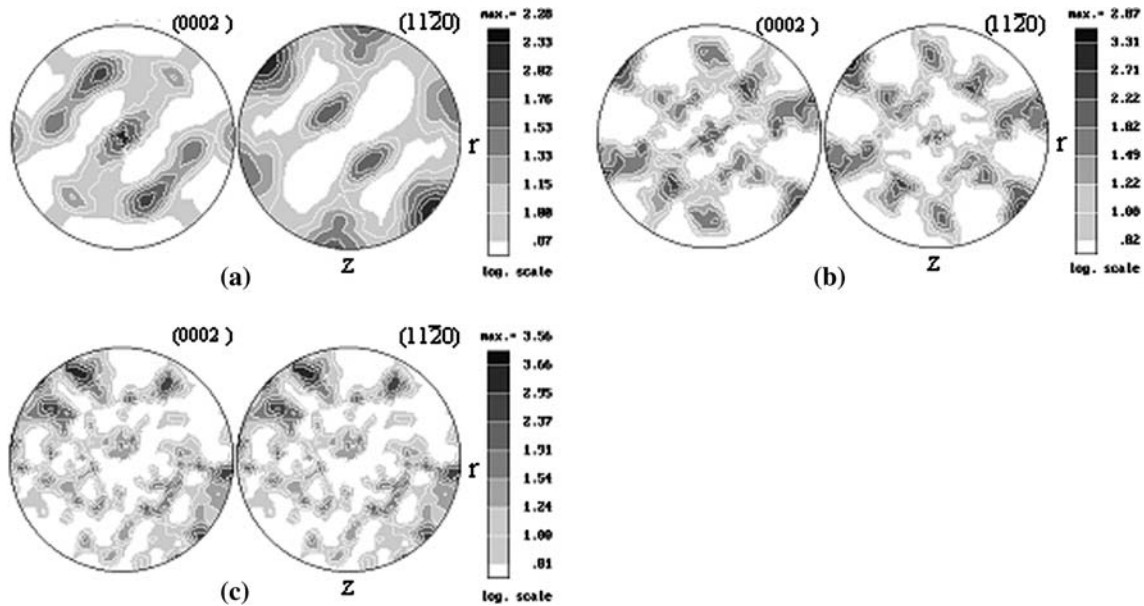


Fig. 7—Alpha-phase pole figures for the RT location following forging and heat treatment: (a) measured, (b) simulated with all variants, and (c) simulated with preferential variant selection based on $\langle 111 \rangle$ pencil-glide.

predict the majority of the features in the measured pole figures, as may be seen in Figure 7(a). When all variants were considered possible (Figure 7(b)), a marked improvement in the correlation was observed. This result is consistent with the microstructure, seen in Figure 4(d), present at this location, in that somewhat random nucleation and growth of the alpha phase would have been expected to occur in the production of the observed basketweave microstructure.

The cooling rate experienced at the RT location was sufficient to produce the orthorhombic (α'') martensitic phase in addition to the secondary-alpha platelets. Based on the lattice parameters of α'' ($a = 3.033$, $b = 4.924$, and $c = 4.667$ Å) deduced in previous X-ray diffraction work,^[31,32] four of the five measured pole figures ((10 $\bar{1}$ 0), (0002), (10 $\bar{1}$ 1), and (11 $\bar{2}$ 0)) for the primary + secondary alpha phase were confounded by the α'' martensitic phase due to diffraction-peak overlap. Moreover, the α'' martensitic phase has a

$$\begin{aligned} (110)_{\beta} // (001)_{\alpha''} \\ [111]_{\beta} // [101]_{\alpha''} \end{aligned} \quad [13]$$

orientation relationship with the β phase,^[33,34] with perhaps its own set of variant-selection criteria for the 12 possible variants. Thus the α'' martensitic phase will be textured in some manner related to the texture of the β phase and may have some effect even at relatively low volume fractions on the calculated orientation distribution function and the recalculated pole figures for the primary + secondary alpha at the RT location, shown in Figure 7(a).

From a quantitative perspective, the model predictions of the alpha-phase texture *intensity* for all locations were reasonably close in some cases and high in

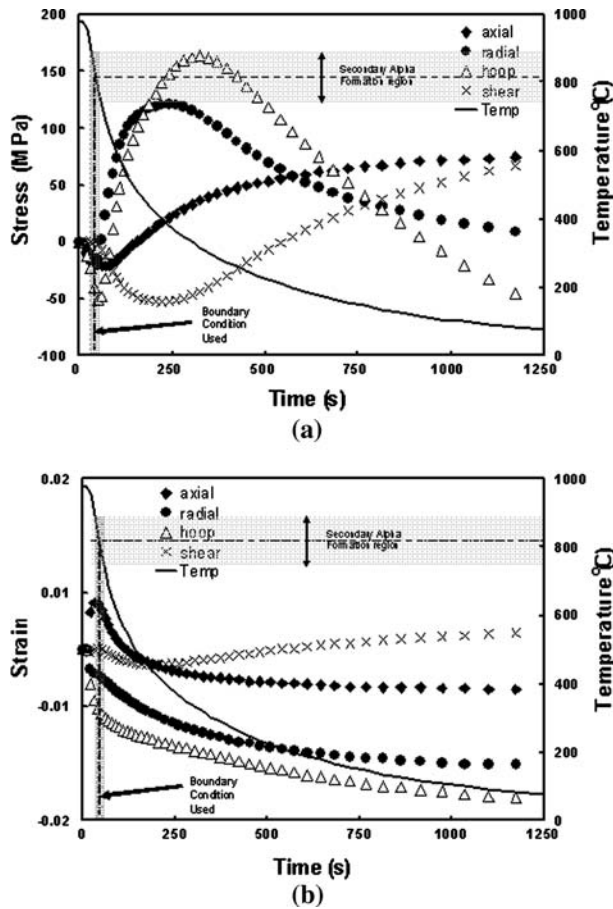


Fig. 8—FEM predictions at the RT location: (a) stress and (b) strain components and temperature as a function of time during water quenching following solution heat treatment of the forging.

others for the variant-selection rules examined. At the BC location (*i.e.*, Figure 5), the predicted texture using all variants, as shown in Figure 5(b), was comparable to the measured texture, Figure 5(a), whereas the modeled texture using the $\langle 111 \rangle$ pencil-glide activity, Figure 5(c), was 4 to 5 times that which was measured. At the RT location, the predicted texture strength using all variants, seen in Figure 7(b), was comparable to the measurement, shown in Figure 7(a). These findings can be rationalized in part due to the fact that Taylor-type models typically predict textures that are *stronger* than those measured. Hence in regions such as location BC, where a large amount of strain is accommodated (Table II), an overprediction in the texture is to be expected and will be compounded by the use of any type of variant-selection biasing criterion that limits which variants form, as seen in Figure 5(b). In addition, the number of discrete orientations which were automatically generated to represent the initial billet texture of the alpha and beta phase in the present work (~ 1000) was insufficient to fully populate the orientation space. As a result, similar to a coarse grain specimen whose texture is measured using X-ray diffraction, the simulated pole figures were spotty, thus limiting the ability to make quantitative texture predictions.

Other differences in the measured-*vs*-predicted pole figures of a quantitative nature may be attributable to the rapid spatial variation in the cooling profiles in specimens close to the outer extremities of the forging. In specimens close to the pancake outer surface, such as the RT specimen, the modeled stresses, cooling rates, and microstructures varied significantly over the surface of the specimen in spite of the large initial billet and final pancake forging dimensions. Moreover, the modeled cooling rates and observed changes in the microstructures

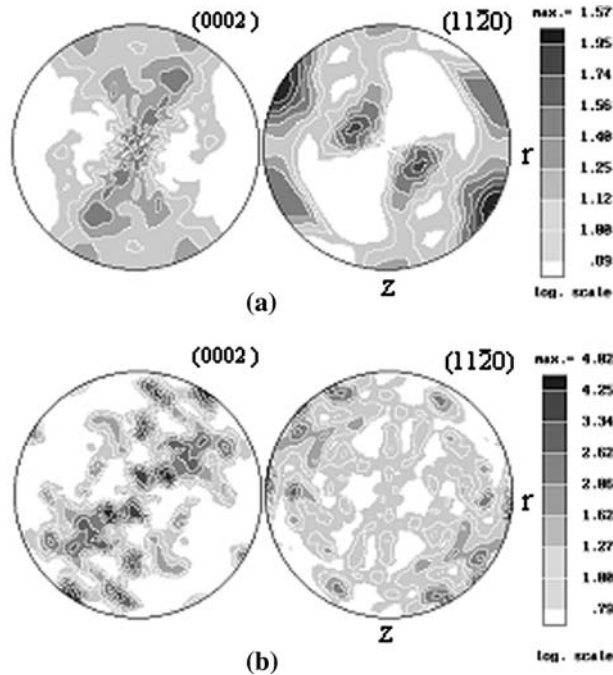


Fig. 9—Primary-alpha pole figures for the RT location following forging + solution heat treatment + furnace cooling: (a) measured and (b) simulated.

developed were consistent with the formation of a low volume fraction of the textured α'' martensitic phase, which would also contribute to the observed quantitative differences in the pole figures.

For specimens at the interior of the pancake forging, such as the BC location, cooling-rate gradients were present, but to a much smaller degree. As a result, the microstructures were relatively homogeneous over the entire sample surface, and the gradients were concluded to play a minor role in the differences in the intensities of the various components of the measured and predicted pole figures.

A comparison of the measured textures for RT samples that were solution treated and furnace cooled (to retain solely the equiaxed alpha phase and its associated deformation texture), shown in Figure 9(a), or water quenched (Figure 7(a)), showed significant differences, thus illustrating the contribution of the transformation texture to the overall alpha-phase texture. Furthermore, the deformation-texture prediction for the furnace-cooled RT sample showed qualitative agreement with the measurement (Figure 9(a) vs Figure 9(b)), but the texture intensity was again approximately twice as strong. Because a Taylor-type crystal plasticity model was used, such a result was again not unexpected.

VI. SUMMARY AND CONCLUSIONS

The development of crystallographic texture during the forging and heat treatment of two-phase (alpha/beta) titanium alloys has been modeled by coupling software to treat strain partitioning between the phases, crystal rotations due to metal flow and slip, and variant selection during the decomposition of beta to form secondary (platelet) alpha. The method was evaluated using an industrial-scale Ti-6Al-4V pancake forging. A comparison of measured and predicted textures showed qualitative and in some cases quantitative agreement. However, several refinements are needed such as improvement in the deformation texture model to reduce the tendency for overprediction of texture intensity and methods to account for possibly competitive variant-selection mechanisms.

ACKNOWLEDGEMENTS

This work was conducted as part of the in-house research of the Metals Processing Group in the Air Force Research Laboratory, Materials and Manufacturing Directorate. The support of the laboratory management and the Air Force Office of Scientific Research (Dr. J.S. Tiley, program manager) are gratefully acknowledged. This project was motivated by the Air Force Metals Affordability Initiative program on Microstructure and Mechanical Property

Modeling for Wrought Titanium Alloys led by the Ladish Company (Cudahy, WI). All of the authors (except SLS) were supported under the auspices of Contract No. F33615-99-2-5215 (Project No. LAD-2). The authors also thank J.D. Miller for experimental assistance.

REFERENCES

1. G.Z. Sachs: *Verein. Deutch Ing.*, 1928, vol. 72, pp. 734–40.
2. G.I. Taylor: *J. Inst. Met.*, 1938, vol. 62, pp. 307–24.
3. Report No. LA-CC-88-6, Los Alamos Polycrystal Plasticity Code, Los Alamos National Laboratory, Los Alamos, NM, 1988.
4. N.R. Barton: Ph.D. Thesis, Cornell University, Ithaca, NY, 2001.
5. E.B. Marin and P.R. Dawson: *Comput. Meth. Appl. Mech. Eng.*, 1998, vol. 165, pp. 23–41.
6. V.C. Prantil, J.T. Jenkins, and P.R. Dawson: *J. Mech. Phys. Solids*, 1995, vol. 43, pp. 1283–302.
7. P. Van Houtte, S. Li, M. Seefeldt, and L. Delannay: *J. Plast.*, 2005, vol. 21, pp. 589–624.
8. R.A. Lebensohn and G.R. Canova: *Acta Mater.*, 1997, vol. 45, pp. 3687–94.
9. B. Commentz, C. Hartig, and H. Mecking: *Comp. Mater. Sci.*, 1999, vol. 16, pp. 237–47.
10. DEFORMTM 2D, version 8.2, Scientific Forming Technologies Corporation, Columbus, OH, 2005.
11. F. Pérocheau and J.H. Driver: *Int. J. Plast.*, 2000, vol. 16, pp. 73–83.
12. S.E. Schoenfeld and R.J. Asaro: *Int. J. Mech. Sci.*, 1996, vol. 38, pp. 661–83.
13. C.S. Lee and B.J. Duggan: *Metall. Mater. Trans. A*, 1991, vol. 22A, pp. 2637–48.
14. S.L. Semiatin, F. Montheillet, G. Shen, and J.J. Jonas: *Metall. Mater. Trans. A*, 2002, vol. 33A, pp. 2719–27.
15. R. Hill: *J. Mech. Phys. Solids*, 1965, vol. 13, pp. 213–22.
16. P.M. Suquet: *J. Mech. Phys. Solids*, 1993, vol. 41, pp. 981–1002.
17. R. Hill: *J. Mech. Phys. Solids*, 1967, vol. 15, pp. 79–95.
18. S.L. Semiatin, S.L. Knisley, P.N. Fagin, F. Zhang, and D.R. Barker: *Metall. Mater. Trans. A*, 2003, vol. 34A, pp. 2377–86.
19. M.G. Glavicic, P.A. Kobryn, T.R. Bieler, and S.L. Semiatin: *Mater. Sci. Eng.*, 2003, vol. A346, pp. 50–59.
20. Z.S. Zhu, J.L. Gu, and N.P. Chen: *Scripta Mater.*, 1996, vol. 34, pp. 1281–86.
21. Z.S. Zhu, J.L. Gu, R.Y. Liu, N.P. Chen, and M.G. Yan: *Mater. Sci. Eng.*, 2000, vol. A280, pp. 199–203.
22. N. Gey and M. Humbert: *Acta Mater.*, 2002, vol. 50, pp. 277–87.
23. N. Gey, M. Humbert, M.J. Philippe, and Y. Combres: *Mater. Sci. Eng.*, 1996, vol. A219, pp. 80–88.
24. N. Gey, M. Humbert, M.J. Philippe, and Y. Combres: *Mater. Sci. Eng.*, 1997, vol. A230, pp. 68–74.
25. H. Moustahfid, M. Humbert, and M.J. Philippe: *Acta Mater.*, 1997, vol. 45, pp. 3785–90.
26. P.R. Morris and S.L. Semiatin: *Text. Cryst. Solids*, 1979, vol. 3, pp. 113–19.
27. H.R. Piehler and W.A. Backofen: *Metall. Trans.*, 1971, vol. 2, pp. 249–55.
28. J.D. Miller and S.L. Semiatin: *Metall. Mater. Trans. A*, 2005, vol. 36A, pp. 259–62.
29. L. Gemain, N. Gey, M. Humbert, A. Hazotte, P. Bocher, and M. Jahazi: *Mater. Characterization*, 2005, vol. 54, pp. 216–22.
30. PANDAT, Computherm LLC, Madison, WI, 2006.
31. M.G. Glavicic and S.L. Semiatin: *Acta Mater.*, 2006, vol. 54, pp. 5337–47.
32. L. Zeng and T.R. Bieler: *Mater. Sci. Eng.*, 2005, vol. A392, pp. 403–14.
33. T.W. Duerig, J. Albrecht, D. Richter, and P. Fisher: *Acta Metall.*, 1982, vol. 30, pp. 2161–72.
34. D. Pionnier, M. Humbert, M.J. Philippe, and Y. Combres: *Acta Mater.*, 1998, vol. 46, pp. 5891–98.